J. Fluid Mech. (2009), *vol.* 635, *pp.* 455–475.
doi:10.1017/S0022112009007903

Interaction of two tandem deformable bodies in a viscous incompressible flow

LUODING ZHU†

Department of Mathematical Sciences, Indiana University–Purdue University Indianapolis, 402 North Blackford Street, Indianapolis, IN 46202, USA

(Received 8 December 2008; revised 27 April 2009; accepted 27 April 2009)

Previous laboratory measurements on drag of tandem rigid bodies moving in viscous incompressible fluids found that a following body experienced less drag than a leading one. Very recently a laboratory experiment (Ristroph & Zhang, *Phys. Rev. Lett.*, vol. 101, 2008) with deformable bodies (rubble threads) revealed just the opposite – the leading body had less drag than the following one. The Reynolds numbers in the experiment were around 10^4. To find out how this qualitatively different phenomenon may depend on the Reynolds number, a series of numerical simulations are designed and performed on the interaction of a pair of tandem flexible flags separated by a dimensionless vertical distance ($0 \leqslant D \leqslant 5.5$) in a flowing viscous incompressible fluid at lower Reynolds numbers ($40 \leqslant Re \leqslant 220$) using the immersed boundary (IB) method. The dimensionless bending rigidity $\hat{K}_b$ and dimensionless flag mass density $\hat{M}$ used in our work are as follows: $8.6 \times 10^{-5} \leqslant \hat{K}_b \leqslant 1.8 \times 10^{-3}$, $0.8 \leqslant \hat{M} \leqslant 1.0$. We obtain an interesting result within these ranges of dimensionless parameters: when Re is large enough so that the flapping of the two flags is self-sustained, the leading flag has less drag than the following one; when Re is small enough so that the flags maintain two nearly static line segments aligned with the mainstream flow, the following flag has less drag than the leading one. The transitional range of Re separating the two differing phenomena depends on the value of $\hat{K}_b$. With Re in this range, both the flapping and static states are observed depending on the separation distance D. When D is small enough, the flags are in the static state and the following flag has less drag; when D is large enough the flags are in the constant flapping state and the leading flag has less drag. The critical value of D depends on $\hat{K}_b$.

1. Introduction

The interaction between a viscous incompressible fluid and a deformable body is ubiquitous in Nature: a flag flapping in the air, a parachute falling in the sky and an eel swimming in the water. In this type of fluid-flexible-structure-interaction problem, the shape of the deformable body can change with time due to the unsteady hydrodynamic forces acting on the bodies; and the changing shape of the bodies, on the other hand, imposes a time-dependent constraint on the local viscous flow (no-slip condition on the non-stationary interfaces between the bodies and the fluid). Due to the unsteady interplay among inertia, body flexibility and hydrodynamic forces, the flexible-structure-fluid-interaction may possess some differing features in contrast with the rigid-body-fluid-interaction. A few such examples were already illustrated

† Email address for correspondence: lzhu@math.iupui.edu

in the literature: the bistability of a one-dimensional flag in a two-dimensional wind (Zhang & Childress 2000), the drag reduction of a flexible fibre in a moving viscous flow (Alben, Shelley & Zhang 2002; Zhu 2008), the spontaneous oscillations of heavy flags in flowing water (Shelley, Vandenberghe & Zhang 2005), the flutter of a flag induced by fluid flow (Argentina & Mahadevan 2005) and the flapping dynamics of a flag in a uniform stream (Connell & Yue 2007). Here in this paper we report another such instance in a more complex setting – two tandem flexible bodies interacting in an incompressible viscous flow.

The presence of multiple deformable objects in a moving viscous fluid complicates the problem further because the deformable objects may interact one another through the ambient moving fluid (sometimes even through direct contact). Some of such examples include: fish schooling in the ocean, birds flocking in the sky and red blood cells aggregating in the flowing blood in human blood vessels. Much research has been done under this direction. Liao *et al.* (2003) demonstrated how a trout might exploit the vortices to reduce the cost of locomotion in the wake of a stationary object in a water flow. Bill & Herrnkind (1973) investigated the drag reduction induced by formation movement of spiny lobsters. Fauci (1990) investigated the interaction of oscillating elastic filaments. Zhu & Peskin (2003) studied the synchronization of two interacting elastic parallel filaments. Zhu & Chin (2008) simulated the interaction of multiple flexible fibres with a pulsatile viscous flow. Farnell, David & Barton (2004) studied the coupled states of flapping flags. Jia *et al.* (2007) studied theoretically and experimentally various coupling modes between two flapping filaments. Dong & Lu (2007) investigated the characteristics of flows past multiple waving flexible foils. Qi & Shyy (2008) simulated the dynamics of free falling of multiple flexible fibres in moderate Re flows. Here we shall discuss simulations of two interacting deformable flags placed in tandem in a moving viscous fluid.

The direct motivation of our work is a recent interesting laboratory experiment on two tandem flapping rubber threads in a two-dimensional viscous flow reported by Ristroph & Zhang (2008). The experiment was conducted in a flow tunnel bounded by two rigid nylon wires with two ends attached to a lifted discharging container of soapy water, and the other two ends attached to a receiving container on the ground. With the switch being turned on, the soapy water flowed down due to gravity along the two wires and formed a thin layer of flowing soap film. Two flexible rubble threads were introduced in tandem at the centre of the tunnel with only their upstream tips fixed. The two threads were separated by a vertical distance D that could be varied. The laboratory measurements revealed that the drag of the downstream flag was greater than that of the upstream flag. This result was surprising because the previous experiments with tandem rigid cylinders (Zdravkovich 1977), race cars (Romberg, Chianese & Lajoie 1971) and energetics of bicyclists (Kyle 1979) had found the opposite: the drag of a trailing object was less than that of a leading one. Presumably this is because the objects in the recent experiment were deformable and those in the previous experiments were rigid. See detailed explanations in § 5.

The Reynolds numbers (Re) in the laboratory experiment were around 10^4. In both the laboratory experiment and our simulations, Re is defined as UL/ν, where U is the inflow speed at the inlet, L is the total length of the flags (all the flags are of equal length) and ν is the fluid kinematic viscosity. To find out how this qualitatively different phenomenon may depend on the Reynolds number, we design and perform a series of numerical simulations on the interaction of two tandem flags separated by a varying distance ($0 \leqslant D \leqslant 5.5$) with a flowing viscous incompressible flow at lower Re (in the range of 40–220) using the immersed boundary (IB) method (Zhu & Peskin 2002; Zhu & Chin 2008). In addition to the Reynolds number, two more important

dimensionless parameters are introduced: the dimensionless flag bending rigidity $\hat{K}_b$ and dimensionless flag mass density $\hat{M}$ which are defined as $\hat{K}_b = K_b/\rho_0 U^2 L^3$ and $\hat{M} = M/\rho_0 L$, respectively. Here K_b is the dimensional flag bending rigidity and M is the mass density of the flag. The number $\hat{K}_b$ characterizes the relative importance between the fluid kinematic energy and the flag elastic potential energy. A smaller value of $\hat{K}_b$ implies a more flexible flag. The number $\hat{M}$ characterizes the relative importance between the fluid inertia and the flag inertia. The values of these parameters used in our work are: $8.6 \times 10^{-5} \leqslant \hat{K}_b \leqslant 8.6 \times 10^{-3}$ and $0.8 \leqslant \hat{M} \leqslant 1.0$. The flags are not neutrally buoyant in the fluid, instead they are heavier than the fluid. Therefore the multigrid version of the IB method (Zhu & Peskin 2002; Zhu & Chin 2008) which can handle massive boundaries are used in our work. For more references on the IB method the readers are referred to the following articles: Peskin (1977), Fauci & Peskin (1988), Fogelson & Peskin (1988), Peskin (1993*a*), Fauci & Fogelson (1993), Roma, Peskin & Berger (1999), Lai & Peskin (2000), Peskin (2002), Wang & Liu (2004), Mittal & Iaccarino (2005), Griffith & Peskin (2005), Atzberger, Kramer & Peskin (2006), Mori & Peskin (2006), Sheldon Wang (2007), Kim & Peskin (2007) and Borazjani *et al.* (2008). For other relevant numerical methods for fluid-structure-interaction, see the references below and therein: the immersed interface method (LeVeque & Li 1994; LeVeque & Li 1997; Li & Lai 2001; Li 2006), the immersed finite element method (Zhang *et al.* 2004; Liu, Kim & Tang 2005), the immersed continuum method (Wang 2006; Sheldon Wang 2007), the level set method (Hou *et al.* 1997; Cottet & Maitre 2004; Cottet & Maitre 2006; Xu *et al.* 2006), the material point method (Sulsky, Chen & Schreyer 1994*a*; Sulsky, Shou & Schreyer 1994*b*), the fictitious domain method (Glowinski, Pan & Periaux 1994*a*,*b*; Glowinski *et al.* 2001), the ghost fluid method (Fedkiw 2002; Fedkiw *et al.* 1999), and the arbitrary Lagrangian–Eulerian method (Hughes, Liu & Zimmerman 1981; Donea, Giuliani & Halleux 1982).

Our numerical simulations reveal an interesting result: when Re is high enough such that the flapping of the flags is self-sustained, the 'inverted' hydrodynamic drafting (hydrodynamic drafting refers to the drag reduction induced by queuing of moving objects in a fluid) is observed, i.e. the drag of the trailing flag is always greater than that of the leading one; when Re is small enough such that the flapping of the flags is not self-sustained (the flags become two static straight segments aligned with the flow after the initial disturbances die out), the hydrodynamic drafting is observed, i.e. the drag of the trailing flag is always less than that of the leading one. The transitional range of the Reynolds number separating these two qualitatively differing scenarios is found to be dependent of the dimensionless bending rigidity $\hat{K}_b$. When the Re falls in such a range, the two flags can stay at either of the two states: the straight static state (hydrodynamic drafting) when D is sufficiently small; the self-sustained flapping state (inverted hydrodynamic drafting) when D is sufficiently large. The critical separation distance D_c is dependent of $\hat{K}_b$. The ranges of the transitional Reynolds number Re_t and the critical distance D_c are determined for two values of the bending modulus through simulations.

In this paper we demonstrate and discuss such three typical cases: the first corresponds to the sustained flapping case ($Re = 165$, 'inverted' drafting); the second corresponds to the static straight case ($Re = 70$, drafting); the third corresponds to the transition case with $Re = 80$.

The remainder of the article is as follows: § 2 addresses a model problem inspired by the laboratory experiment conducted in Ristroph & Zhang (2008); § 3 gives the corresponding IB mathematical formulation for the model problem; § 4 briefly talks about the discretization and solution method of the mathematical formulation and

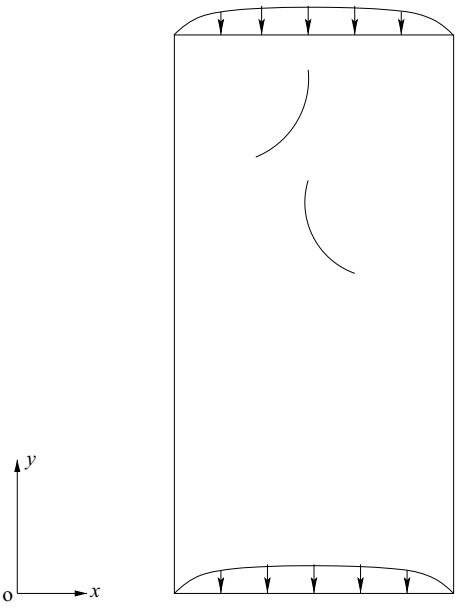

FIGURE 1. A diagram of the model problem. The black rectangle represents the computational domain. The positive x-axis points from left to right along the width direction, and the positive y-axis points from bottom to top along the height direction. The gravity acts along the negative y-axis, and the fluid flows from top to bottom. The two black curves represent two flags. The upper tips of the flags are fixed. No other parts are restricted. The curves on inlet (top) and outlet (bottom) represent the inlet/outlet velocity profile. The arrows represent the magnitude of the velocity.

§ 5 discusses the details of the simulation results. The § 6 concludes the article with a summary and discussion.

2. A model problem

Idealized and simplified from the laboratory experiment (Ristroph & Zhang 2008), a model problem is set up as follows for the study of fluid-deformable-flag-interaction (see figure 1 for a diagram). We consider a viscous incompressible flow past a pair of flexible flags placed in tandem at the centre of a two-dimensional rectangular domain with aspect ratio 2:1 (height to width). The fluid is Newtonian, and the flags are linear elastic. The fluid is driven by gravity and flows from top to bottom (along the negative direction of y-axis). The same velocity profile (i.e. the initial velocity evaluated on a fixed y coordinate) is specified at the inlet and outlet boundary (top and bottom). The no-slip condition is used on the two side rigid walls (left and right, i.e. x direction). The upstream two tips of the two flags are fixed, and no other parts are restricted. The pair of flags is separated by a distance D along y direction between the free-tip of the upper flag and the fixed-tip of the lower flag which is measured when the flags are static and straight. No separation distance is allowed along the x direction. The initial velocity is the velocity field that satisfies the steady viscous incompressible Navier–Stokes equations with two external forcing terms (gravity and air drag) on a two-dimensional rectangular domain (finite width and infinite height) using the no-slip condition on the two side boundaries.

3. The IB mathematical formulation

The IB method we employ for our fluid-flexible-flag problem is the version described in (Zhu & Peskin 2002; Zhu & Chin 2008). The IB mathematical formulation for our model problem is non-dimensionalized by three reference quantities (the inflow speed U, the fluid mass density ρ_0 and the flag length L). The dimensionless IB formulation in component form reads as follows:

$$\rho(x,y,t)\left(\frac{\partial u}{\partial t}+u\frac{\partial u}{\partial x}+v\frac{\partial u}{\partial y}\right)=-\frac{\partial p}{\partial x}+\frac{1}{Re}\left(\frac{\partial^2 u}{\partial x^2}+\frac{\partial^2 u}{\partial y^2}\right)+f_x(x,y,t)-\lambda u, \quad (1)$$

$$\rho(x,y,t)\left(\frac{\partial v}{\partial t}+u\frac{\partial v}{\partial x}+v\frac{\partial v}{\partial y}\right)=-\frac{\partial p}{\partial y}+\frac{1}{Re}\left(\frac{\partial^2 v}{\partial x^2}+\frac{\partial^2 v}{\partial y^2}\right)+f_y(x,y,t)-\lambda v-\gamma, \quad (2)$$

$$\frac{\partial u}{\partial x}+\frac{\partial v}{\partial y}=0, \quad (3)$$

$$\rho(x,y,,t)=1+\int_\Gamma \tilde{M}\delta(x-X(\alpha,t))\delta(y-Y(\alpha,t))\,\mathrm{d}\alpha, \quad (4)$$

$$f_x(x,y,t)=-\int_\Gamma \frac{\partial \mathscr{E}}{\partial X}\delta(x-X(\alpha,t))\delta(y-Y(\alpha,t))\,\mathrm{d}\alpha, \quad (5)$$

$$f_y(x,y,t)=-\int_\Gamma \frac{\partial \mathscr{E}}{\partial Y}\delta(x-X(\alpha,t))\delta(y-Y(\alpha,t))\,\mathrm{d}\alpha, \quad (6)$$

$$\mathscr{E}=\frac{1}{2}\hat{K}_s\int_\Gamma\left(\sqrt{\left(\frac{\partial X}{\partial \alpha}\right)^2+\left(\frac{\partial Y}{\partial \alpha}\right)^2}-1\right)^2\mathrm{d}\alpha+\frac{1}{2}\hat{K}_b\int_\Gamma\left(\left(\frac{\partial^2 X}{\partial \alpha^2}\right)^2+\left(\frac{\partial^2 Y}{\partial \alpha^2}\right)^2\right)\mathrm{d}\alpha, \quad (7)$$

$$\frac{\partial X}{\partial t}(\alpha,t)=\int_\Omega u\delta(x-X(\alpha,t))\delta(y-Y(\alpha,t))\,\mathrm{d}x\,\mathrm{d}y, \quad (8)$$

$$\frac{\partial Y}{\partial t}(\alpha,t)=\int_\Omega v\delta(x-X(\alpha,t))\delta(y-Y(\alpha,t))\,\mathrm{d}x\,\mathrm{d}y. \quad (9)$$

In above equations, x and y are the Eulerian coordinates associated with the fixed computational domain, α is the Lagrangian coordinate associated with the moving flags and t is the time. The ρ is Eulerian mass density of the fluid and the flags. The u and v are the components of the fluid velocity along x and y axes, respectively. The p is pressure, Re is the Reynolds number. The f_x and f_y are the components of the Eulerian force density along x and y axes, respectively, which are associated with the forces applied by the flags to the surrounding fluid. The λ is the dimensionless air drag coefficient and γ is the dimensionless gravitational constant, both of which happen to be the reciprocal of the Froude number Fr for our problem after non-dimensionalization: $\lambda=\gamma=1/Fr$, where the Froude number $Fr=U^2/gL$, here g is the dimensional gravitational acceleration constant. The symbol Γ represents the flags, and the symbol Ω represents the two-dimensional fluid domain (the rectangle with an aspect ratio of 2:1). The Eulerian mass density ρ is computed by (4) where $\tilde{M}$ is the difference in mass density of the flag and the fluid, and δ is the Dirac delta function. The Eulerian force density is computed by (5) and (6) where $\mathscr{E}$ is the elastic potential energy density associated with the flags, and X and Y are the Eulerian coordinates (x and y components, respectively) of the flags whose associated Lagrangian coordinate is α. The elastic energy stored in the flags is generated by stretching/compression (the first term in (7)) and bending (the second term in (7)).

Here $\hat{K}_s$ and $\hat{K}_b$ are the stretching/compression coefficient and bending modulus of the flags. The flag position (X, Y) is updated by (8) and (9).

4. Discretization of the IB formulation

The above IB formulation (defined in (1)–(9)) is discretized by a finite difference method on a series of gradually coarsened fixed grids. Because the mass density $\rho(\mathbf{x}, t)$ varies with space and time in our case, the discrete FFT frequently utilized by the IB method is no longer appropriate. Instead, a geometrical multigrid method (seven-gird V-cycle) is employed to solve the formulation. The finest grid has a resolution of 256 (x direction) by 512 (y direction) grid points, the coarsest grid has a resolution of 4 by 8 grid points. Each of the flags is represented by a collection of 116 moving Lagrangian points. The Navier–Stokes equations are discretized by Chorin's projection method (Chorin 1968, 1969) generalized to the case of variable mass density. We refer readers interested in this method to the following papers and references therein: (Bell, Colella & Glaz 1989; Bell, Colella & Howell 1991; Perot 1993; Weinan & Liu 1995, 1996; Botella 1997; Lopez & Shen 1998; Brown, Cortez & Minion 2001; Lopez, Marques & Shen 2002). The nonlinear term is linearized by taking advantage of the velocity field at the previous time step, and the skew-symmetrical scheme is used for its discretization. The IB force is computed explicitly. The time derivative is discretized by the forward Euler scheme and the spatial derivatives are discretized by the centred difference scheme. The Dirac delta function is approximated by the 4-point δ_h involving the cosine function (Peskin 2002). The δ_h is defined at each discrete point of the flags, and has a support of a square consisting of 4×4 fixed Eulerian grid points. See (Zhu & Peskin 2002; Zhu & Chin 2008) for details of the discretization and the solution processes.

5. Major numerical results

Before the numerical results are discussed, we would like to address how the drag is defined and computed in our simulations. The drag of the tethered flag is defined as the integral of the y component (vertical) force applied by the fluid to the flag along the flag. In the IB method, the instantaneous drag (D_f) each tethered flag experiences can be conveniently computed as the y component of the tension at the flag tethered point. The reason is as follows. In the IB method the flag is represented by a collection of Lagrangian moving points. The upper flag endpoint is tethered to a fixed Eulerian point (i.e. its coordinates are constant depending on where the flag is tethered) by a stiff virtual spring. The dimensionless spring stiffness (defined as $K/\rho_0 U^2 L$ where the K is the dimensional spring constant) is chosen to be very large (1.2×10^7 in our case) such that the maximum of $|\mathbf{d}|$ ($\mathbf{d}$ is the displacement of the flag upper endpoint) is nearly zero (less than or equal to 0.1 % of the flag total length in our case). Thus the flag is almost 'fixed' to the Eulerian point. The tension at the 'fixed' flag endpoint equals the product of the displacement and the spring stiffness. By the Newton's second law, this tension is just equal to the summation of the forces applied by the fluid to the flag defined at all the flag Lagrangian points because the flag mass is spread to the fluid and enters into the Navier–Stokes equations.

Because the flow is unsteady, the instantaneous drag D_f varies with time. To remove the unsteadiness in the instantaneous drag, an averaged drag ($\bar{D}$) is computed as a time average over N equally spaced instants between time T_1 and T_2. The T_1 and T_2

are the beginning and ending instants of drag average, respectively. The time T_1 is chosen such that the initial disturbances on the flags have died out and the flags have reached either a self-sustained flapping state or a stationary state. The values of T_2 and N are chosen arbitrarily. In this work $N = 400$, $T_1 = 10$, $T_2 = 50$.

A series of simulations are performed on two tandem interacting flags separated by a varying distance D immersed in a moving viscous fluid with Reynolds number in the range 40–220. The dimensionless parameters used for this work are as follows: the fluid density $\rho_0 = 1.0$, the flag length $L = 1.0$, the inflow speed $U = 1.0$, the flag mass density $\hat{M} = 0.8$–1.0, the flag bending modulus $\hat{K}_b = 8.6 \times 10^{-5}$–$8.6 \times 10^{-3}$, the stretching coefficient $\hat{K}_s = 8.2 \times 10^7$, the Froude $Fr = 24.7$, the Reynolds number $Re = 40$–220, the flag vertical separation $D = 0$–5.5 and the width and height of the computational domain is 5 and 10, respectively.

We find an interesting result on the drag of the two flags: when Re is sufficiently high such that the two flags flutter sustainedly, the drag of the leading flag is always less than the trailing flag (i.e. the leading flag enjoys a drag reduction); when Re is sufficiently small such that the flags maintain two static line segments in the flowing fluid after the initial oscillation is completely damped, the drag of the leading flag is always greater than the trailing flag (i.e. the trailing flag enjoys a drag reduction). The transitional range of the Reynolds number separating these differing behaviour is found to be dependent of the flag bending rigidity $\hat{K}_b$. For Re in such a range, the motion and drag of the flags depend on a critical separation distance D_c: when $D < D_c$, the flags settle down to a straight static state after the initial disturbances die out and the downstream flag has less drag than the upstream flag; when $D > D_c$, the two flags settle down to a self-sustained flapping state and the upstream flag has less drag than the downstream one. The value of D_c varies with $\hat{K}_b$. The intervals of Re_t and D_c are determined via computations for two typical values of $\hat{K}_b$.

In this paper we demonstrate three typical such cases: a fluttering case with $Re = 165$, a stationary case with $Re = 70$ and a transition case with $Re = 80$. For the three cases all the parameters except Re are the same. The flag mass density $\hat{M} = 0.87$, the flag bending modulus $\hat{K}_b = 8.6 \times 10^{-4}$ (see above for other dimensionless parameters used for the three cases). For each case, we discuss the drag of the two flags as a function of the separation distance D, the envelopes of the flags versus D (fluttering case only) and some typical flow visualization (fluid motion and the vortical field). The account of the numerical results are accompanied by physical explanations whenever possible.

First, the flapping case with $Re = 165$. Figure 2 plots the dimensionless drag versus the separation distance D. The drag of the two flags is non-dimensionalized by the drag d_0 of a single flag flapping in the viscous flow (all the flow and flag parameters used for computing d_0 are the same as in the two-flag case). The flag separation distance D is non-dimensionalized by the flag length L. The triangles ('△') represent the drag of the leading flag, the squares represent the drag of the trailing flag and the circles ('o') represent the total drag of the flags (i.e. the sum of the drag of the two flags). We can see that the drag of the trailing flag is always greater than that of the leading one for the range of D in 0–5.5. Compared to the single-flag case, the leading flag enjoys a drag reduction while the trailing one undergoes a drag increase (except for $D = 0$ and 0.1 where both flags experienced a drag reduction). The total drag of the flags is reduced (i.e. the total drag is less than 2) only for a small separation distance ($D = 0$ and 0.1). For greater values of D the two flags as a whole experiences a drag increase: the total drag is greater than twice of the drag of the single flag, i.e. the total drag is more than 2.

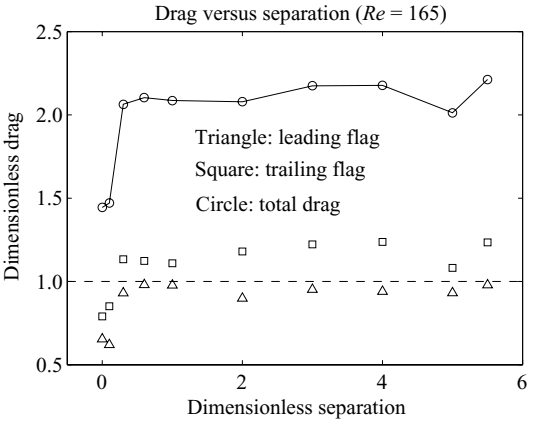

FIGURE 2. Drag versus separation distance for $Re = 165$. The x-axis is the flag separation distance D (dimensionless). The y-axis is the dimensionless drag. The dashed line represents the drag of a single flag. The triangles represent drag of the upper flag, the squares represent drag of the lower flag and circles represent the total drag of the flags.

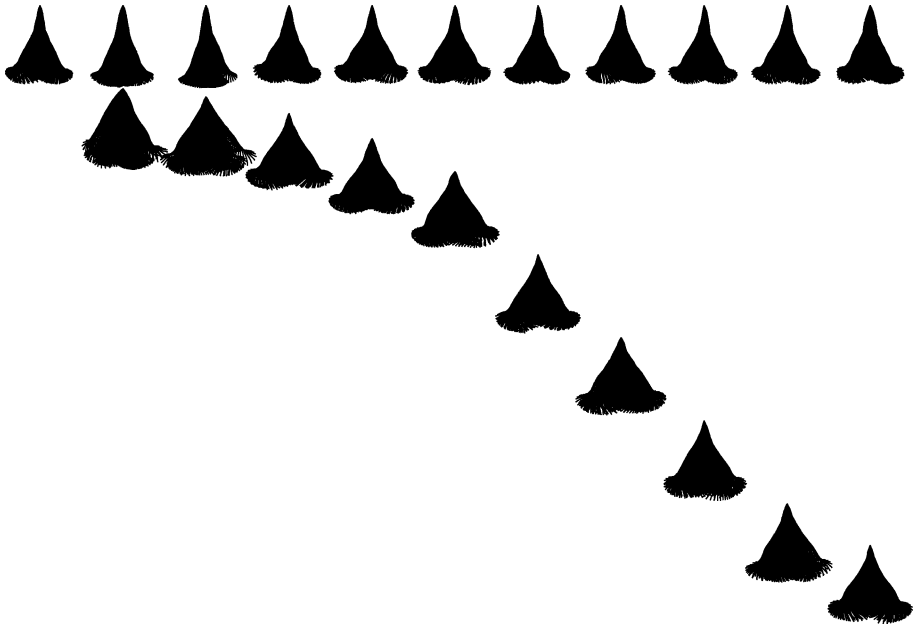

FIGURE 3. The envelopes of the flags versus the separation distance for $Re = 165$. The first row represents the upstream flag, and the remaining represents the downstream flag. The leftmost envelope corresponds to the single-flag case. The remaining ones corresponds to the two-flag case. The separation distance D is, starting the second column, 0, 0.1, 0.3, 0.6, 1, 2, 3, 4, 5, 5.5, from left to right, respectively. For each column the vertical distance is proportional to the actual flag separation distance D. The space between neighbouring columns is an arbitrary constant.

Figure 3 plots the envelopes of the flags versus separation distance D. The first row represents the upstream flag, and the remaining represents the downstream flag. The leftmost envelope corresponds to the single-flag case. The remaining ones correspond to the two-flag case. The separation distance D varies from 0 (the second column)

to 5.5 (the last column). The remaining values of D are 0.1, 0.3, 0.6, 1, 2, 3, 4, 5, from left to right, respectively. For each column the vertical distance is proportional to the actual flag separation distance D. The space between neighbouring columns is a constant taken arbitrarily. We see that the envelope of the trailing flag is always broader than that of the corresponding leading one. This may explain why the trailing flag experiences greater drag. Notice that the size and shape of the envelope of the leading flag is roughly the same and all look similar to the single-flag case when the separation distance is large enough ($D \geqslant 0.3$). This seems to indicate the influence of the downstream flag weakens as D is increased. As a result the drag of the leading flag is nearly constant for $D \geqslant 0.3$. For the same range of D, the size and shape of the trailing flag all look similar to one another as well. When $D = 0$ and 0.1, the envelopes of the leading flag are slightly smaller compared to the corresponding case for greater values of D. The size of the trailing flag is slightly narrower when $D = 0$ and slightly broader when $D = 0.1$, compared to those when D is greater. This differing behaviour of the leading flag for $D = 0$ and 0.1 may be explained by the local suppression effect of the fixed-tip of the trailing flag on the motion of the free-end of the leading flag: the localized vortices around the fixed-point may hinder the passage of the free-tip of the leading flag. Thus the size of envelope of the leading flag becomes smaller, and the drag is decreased when $D = 0$ and 0.1.

The flag fluttering-frequency in the single-flag case is approximately 0.43, the flapping amplitude is approximately 0.75. This frequency is inherited by the two-flag system for sufficient large separation distance: each of the two flags flutter at the same frequency (approximately 0.43) when $0.3 \leqslant D \leqslant 5.5$. When $D = 0$ and 0.1, however, the frequency of the upper flag is approximately 0.29 and that of the lower flag is approximately 0.32. The downstream flag is immersed in the wake of the upstream flag and its flapping motion is caused by the oscillating wake generated by the leading flapping flag. Because the flag is passive, it simply oscillates with the wake. Therefore the downstream flag inherits the flapping frequency of the upstream flag. The loss of resonance for $D = 0$ and 0.1 is probably caused by the strong interaction between the free-tip of the upper flag and the local vortices around the fixed tip of the lower flag. The amplitude (the maximum displacement of the free-tip along x direction) of each of the two flags is roughly a constant for the range of separation distance D considered here. It is approximately 0.75 for the upper flag and approximately 1.0 for the lower flag. (The amplitude of the upper flag is slightly smaller for $D = 0$ and 0.1; that of the lower flag is slightly smaller for $D = 0$ and slightly bigger for $D = 0.1$.)

While the larger flapping amplitude of the lower flag is responsible for the greater drag it experiences, it is not apparent why the lower flag would have a larger flapping amplitude than the upper flag. A mathematical explanation seems to be out of question given the complexity of the nonlinear system that governs the problem at finite Reynold numbers. An intuitive physical explanation is offered as follows. The flags are passive and they simply follow the motion of the surrounding fluid because of fluid viscosity. While a majority of the upstream flag is surrounded by a nearly uniform flow the downstream flag is entirely immersed in the wake of the upstream flag. The flapping motion of the upper flag generates a disturbed vortex-embedded wake which oscillates with the upper flag (as can be seen from a simulation animation). The oscillatory wake is beneficial to the flapping motion of the downstream flag. This may explain why the downstream flag has a broader flapping amplitude than the upstream one.

Figure 4 demonstrates a typical visualization of the flow and the flags for $D = 0$. The top figures plots the instantaneous positions of massless fluid markers introduced

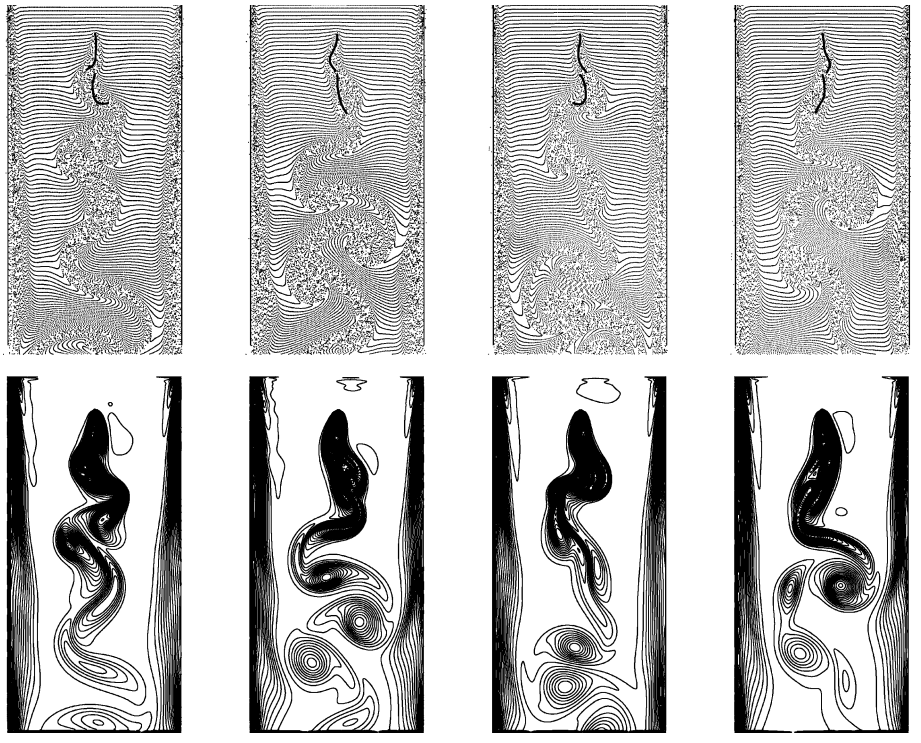

FIGURE 4. Visualization of the flow and the flags for $Re = 165$ and separation distance $D = 0$. The upper panel plots the instantaneous positions of fluid markers. The lower panel plots the vorticity contours. Each column corresponds to a different time instant. The dimensionless time is 13.75, 16.5, 19.25 and 22, from left to right, respectively.

along the inlet boundary and carried away by the flowing fluid. The bottom figures plots the vorticity contours from which vortices can be seen. Each column (markers and contours) corresponds to a different time instant. Although the two flags share the same flutter frequency, the phase difference is clearly shown in the top figures: at $t = 13.75$ the leading flag moves towards the right while the trailing one moves towards the left; at $t = 19.25$ the leading flag moves towards the left while the trailing one moves towards the right; At the other two instants the flags move towards the same side but with perceivable phase difference. It is interesting to notice that the wake of the flags is narrowed when the two flags move towards different directions (the first and third figures on top) and accordingly the shed vortices are flattened (the corresponding figures on bottom); the wake is widened when they move towards the same direction (the second and the fourth figures on top) and accordingly the shed vortices are circulated (the corresponding figures on bottom). Figure 5 demonstrates a typical visualization of the flow and the flags for $D = 1$ for four different time instants. An animation based on the simulation results shows that the two flags separated by $D = 1$ have less phase difference than the case of $D = 0$: they flutter always along the same direction with a roughly constant phase difference. (See top figures: the flags fluttered towards the left in the first three figures, and they flutter towards the right in the fourth figure.) Consequently, the wake is wider and shed vortices are much closer to being circular compared to the $D = 0$ case. Also the shed vortices are more or less discrete rather than somewhat attached to one another in the previous case.

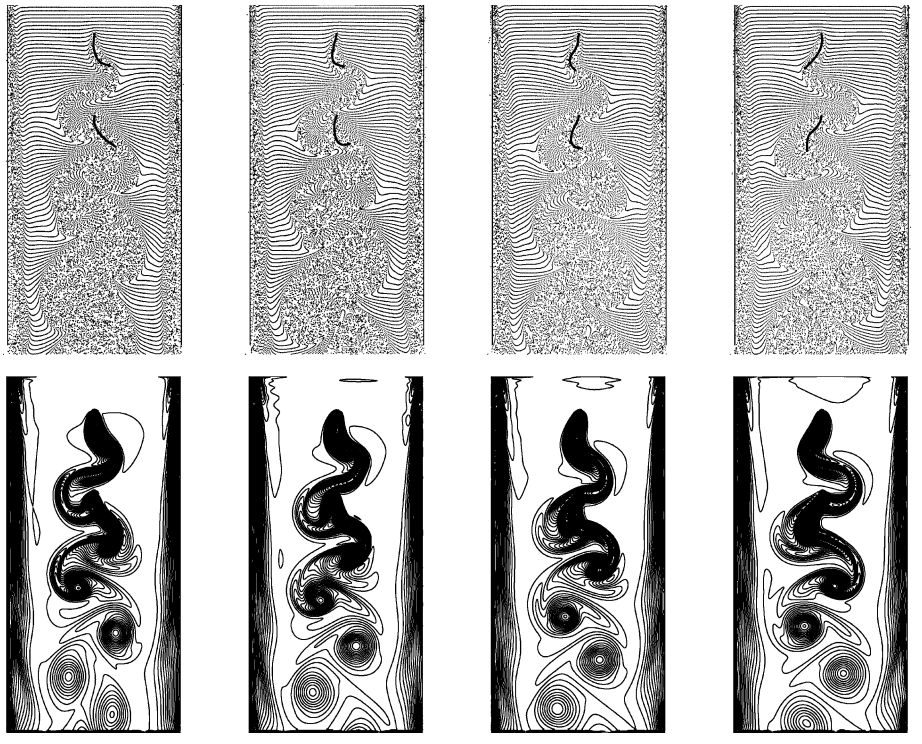

FIGURE 5. Visualization of the flow and the flags for $Re = 165$ and separation distance $D = 1$. The upper panel plots the instantaneous positions of fluid markers. The lower panel plots the vorticity contours. Each column corresponds to a different time instant. The dimensionless time is 13.75, 16.5, 19.25 and 22, from left to right, respectively.

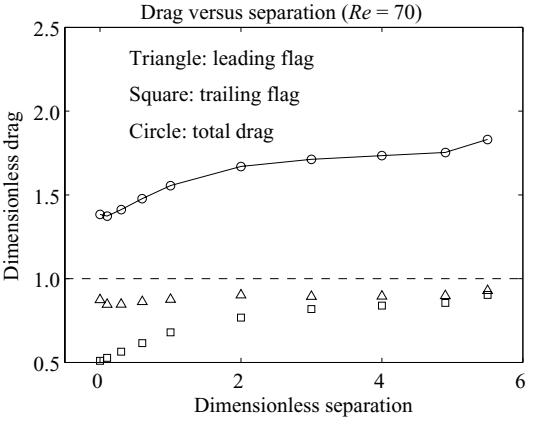

FIGURE 6. Drag versus separation distance for $Re = 70$. The x-axis is the flag separation distance D (dimensionless). The y-axis is the dimensionless drag. The dashed line represents the drag of a single flag. The triangles represent drag of the upper flag, the squares represent drag of the lower flag and circles represent the total drag of the flags.

Now let us look at a typical non-flapping case with $Re = 70$. Figure 6 and figure 7 display some typical results when self-sustained fluttering no longer occur. Figure 6 plots the drag of the two flags versus the separation distance. All the symbols used

for this figure are the same as those used in figure 2. Interestingly we see that the drag of the leading flag is always greater than that of the trailing one for the range of D in 0–5.5. Compared to the single-flag case, both of the flags enjoy a drag reduction, and the total drag is less than 2 for all the separation distance. This result is in sharp contrast with the fluttering case, and is in agreement with previous results for rigid bodies (Romberg *et al.* 1971; Zdravkovich 1977; Kyle 1979). Notice that the drag of the trailing flag gradually increases with the increase of separation distance and appear to converge to the drag of the leading one, which is not seen at the higher Re flapping case. This seems to suggest that the interaction of the two flags at lower Re is weaker in general. The weakening appears to be caused by the increased damping viscous force as Re is decreased.

Presumably, the vanishing self-sustained flapping for a fixed value of $\hat{K}_b$ is caused by the decreasing of Re which renders the viscous force more and more important than the inertial force. The dominating viscous force causes damping of the flag oscillation and makes the flapping not sustainable. Because the flags remain nearly straight aligned with the flow, the shape drag is not significant. The drag the flag bears is mainly the viscous force acting on the flags which is proportional to the magnitude of velocity gradient $\partial v/\partial x$ (velocity $\mathbf{u}=(u, v)$) on the flags. The downstream flag is surrounded by the wake of the upstream flag where the vertical momentum is decreased compared to the upstream flag whose upper part is enclosed by the uniform oncoming flow. Noticing the no-slip boundary condition on the flags, the velocity gradient magnitude $|\partial v/\partial x|$ is therefore smaller for the downstream flag than the upstream one. As a consequence the drag is reduced for the downstream flag. Note that the mechanism of hydrodynamic drafting for the flags in the static case is different from that in (Romberg *et al.* 1971; Zdravkovich 1977; Kyle 1979). The physics of the hydrodynamic drafting observed in (Romberg *et al.* 1971; Zdravkovich 1977; Kyle 1979) may be as follows. The trailing body is submerged in the wake of the leading one where the pressure is reduced. The reduced pressure on the front of the trailing body (in contrast with the pressure on the front of the leading body) causes the reduction of the form drag for the trailing body. The skin friction for the two bodies is roughly the same. Therefore the total drag of the trailing body is reduced compared to the leading one. In the case of two flapping flags, the downstream flag is nearly aligned with the wake (rather than somewhat lateral to the wake as the bodies in Romberg *et al.* 1971; Zdravkovich 1977; Kyle 1979 were). Both sides of it are exposed to low pressure in the wake. Therefore the above drafting mechanism does not apply to the flag case.

Figure 7 demonstrates some typical visualizations for the flow and the flags. The upper panel plots the instantaneous fluid marker positions and the lower panel plots the vorticity contours for four different values of D. The first column (top and bottom figures) corresponds to $D=0$, the second column $D=0.3$, the third $D=1$ and the fourth $D=4$. From animations based on the simulations we can see that, in all the cases, after the oscillations induced by the initial disturbances on the flags are gone, the two flags maintain two nearly static line segments aligned with the flow. The flags are not strictly straight because they are flexible. The downstream flag causes widening of the wake starting near the fixed-tip of the downstream flag. It seems that the wake and vortices corresponding to different values of D are similar to one another in the sense that one picture may be constructed roughly through a vertical translation of another by an appropriate distance. Again this indicates that the interaction between the two flags in the non-flapping case is weaker because of the lowered Re.

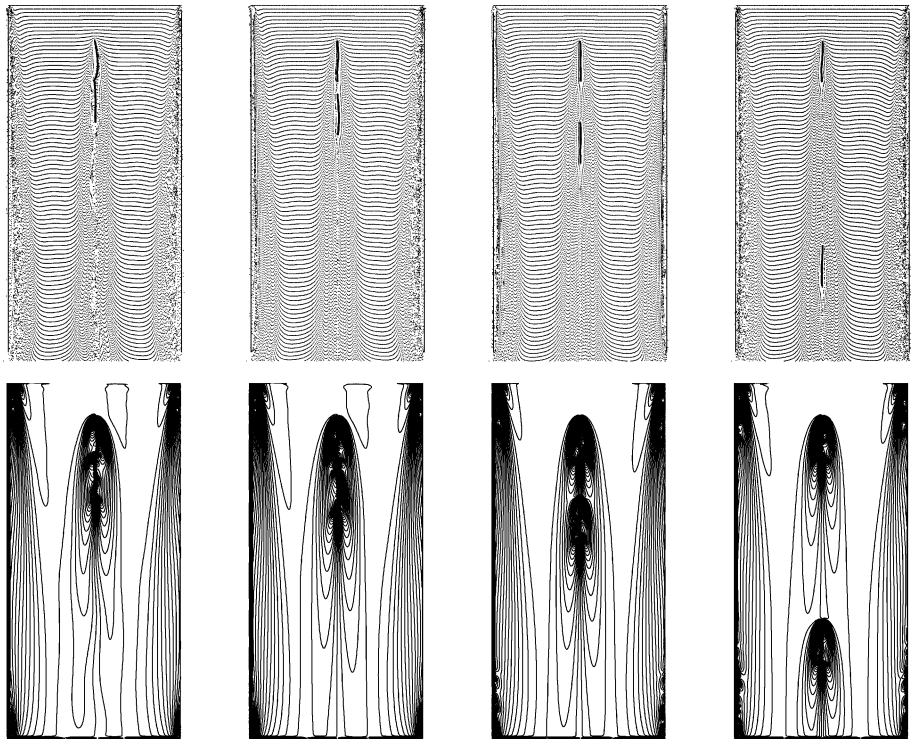

FIGURE 7. Visualization of the flow and flags for $Re = 70$. The upper panel plots the instantaneous positions of fluid markers. The lower panel plots the vorticity contours. Each column corresponds to a different separation distance. The value of D is 0, 0.3, 1, 4, from left to right, respectively. The dimensionless time is 27 for each case.

Notice that in both scenarios (flapping and non-flapping), the upper flag has less drag than that of the corresponding single-flag case (the upper-flag drag <1). Presumably this is caused by the presence of the downstream flag that serves as an obstacle for the upstream flow. This incurs additional resistance to the upstream flow compared to the single-flag case. The deterred mainstream flow presents less drag for the upper flag. It appears that this influence is strong when $D = 0$ and 0.1, and becomes weak as D increases. Also this influence is weaker in the non-flapping case. However, it seems that the hindered upstream flow does not have significant influence on the flapping frequency, amplitude and envelope of the upper flag once the separation distance D is large enough ($D \geqslant 0.3$).

Finally, we address a typical transition case with $Re = 80$. Figure 8 and figure 9 display some typical results. Figure 8 plots the drag of the two flags versus the separation distance. All the symbols used for this figure are the same as those used in figure 2. We can see from the figure that: when D is relatively small, the trailing flag has less drag than the leading flag and both flags experience a drag reduction compared to the single-flag case, therefore the total drag is less than 2; when D is larger, however, the leading flag has less drag than the trailing one and both flags experience a drag increase than in the single-flag case, therefore the total drag is greater than 2. It appears that the transition between these two scenarios is not gradual in D: it jumps from one to the other for some critical value of D in (0.7, 0.8). This may be explained as follows: there exist no other states for the two flags; either both flags flap sustainedly or both flags become static straight lines aligned with the

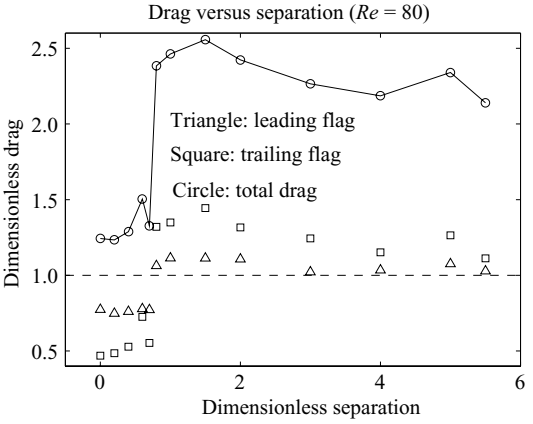

FIGURE 8. Drag versus separation distance for $Re = 80$. The x-axis is the flag separation distance D (dimensionless). The y-axis is the dimensionless drag. The dashed line represents the drag of a single flag. The triangles represent drag of the upper flag, the squares represent drag of the lower flag and circles represent the total drag of the flags.

main flow. In the former case, the leading flag has less drag; in the latter case, the trailing flag has less drag. Therefore the transition on the drag-distance plot shows a jump. One may argue that the following scenarios are also possible: the leading flag in the flapping state and the trailing flag in the static state; or the leading flag in the static state and the trailing flag in the flapping state. But according to our simulations, this is not the case. The reason may be as follows. When the leading flag flaps sustainedly, it generates a constantly oscillating wake which facilitates the flapping of the trailing flag embedded in the wake. Hence a constantly flapping leading flag causes the trailing flag to flap constantly as well. When the leading flag settles down into a static state, the wake behind it is non-oscillatory and much narrower than in the flapping case. This seems to restrict the flapping motion of the embedded trailing flag. Hence a static leading flag tends to make the trailing flag static as well. Note that in our problem the two flags are identical.

Figure 9 visualizes the motion of the flag-fluid system for four different values of D. All the parameters in the four simulations are the same except the separation distance D. The top panel demonstrates the motion of the fluid particles and the flags and the bottom panel demonstrates the motion of the vortices and the flags. Each column (top and bottom figures) corresponds to a simulation with different separation distance: $D = 0$, 0.7,0.8, 2.0, from left to right, respectively. The time instant is 66 (dimensionless) for each simulation. It can be seen that when $D = 0$ or 0.7, both flags settle down to the straight-line state where the flags are nearly static and aligned with the mainstream flow, and the hydrodynamic drafting is observed; when $D = 0.8$ or 2, both flags settle down to a flapping state where the flags oscillate sideway constantly, and the inverted hydrodynamics is observed.

The critical separation distance D_c is between 0.7 and 0.8 for this series of simulations ($Re = 80$). We find that the value of D_c remains within in this range when Re is varied within the transitional Re range (77–84) for this set of simulations ($\hat{K}_b = 8.6 \times 10^{-4}$, $\hat{M} = 0.87$).

As already discussed in the flapping case, a small separation distance D may hinder the flapping motion of the leading flag (eventually the flapping of the trailing flag as well since a static leading flag tends to induce a static trailing flag). When D is

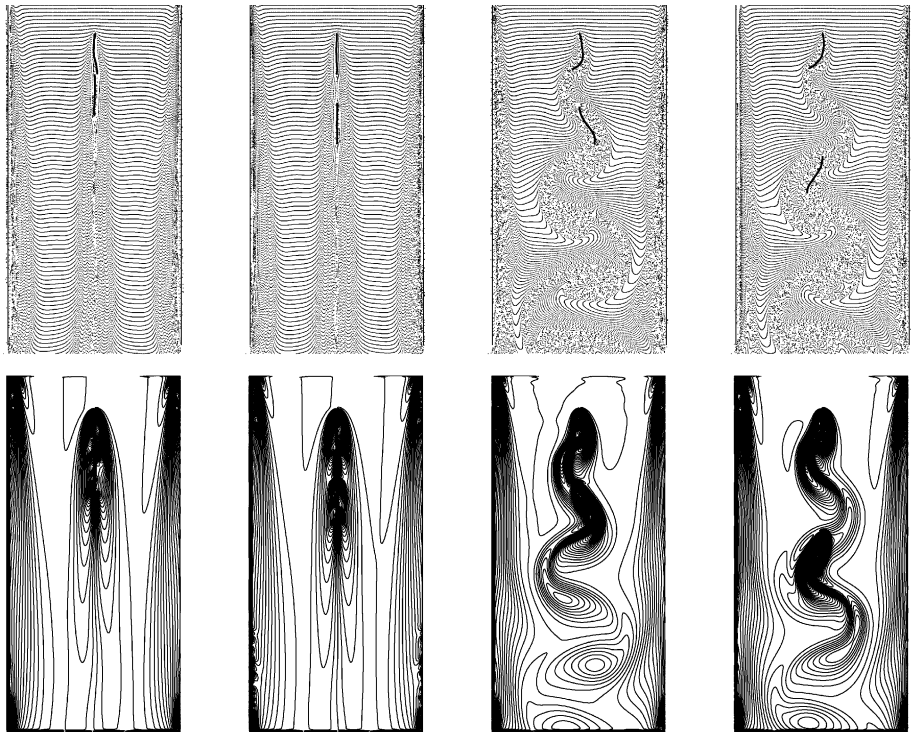

FIGURE 9. Visualization of the flow and flags for $Re = 80$. The upper panel plots the instantaneous positions of fluid markers. The lower panel plots the vorticity contours. Each column corresponded to a different separation distance. The value of D is 0, 0.7, 0.8, 2, from left to right, respectively. The dimensionless time is 66 for each case.

$\hat{K}_b$	8.6×10^{-5}	8.6×10^{-4}	$\geqslant 2.8 \times 10^{-3}$
Re_t	(45, 50)	(77, 84)	>220
D_c	(0.9, 1.0)	(0.7, 0.8)	N/A

TABLE 1. Re_t and D_c versus $\hat{K}_b$.

small, the wake of the oscillating leading flag may not have enough time and space to evolve into a fully developed oscillating wake before it encounters the trailing flag which may weaken the oscillatory motion of the leading flag. This seems to restrict the flapping motion of both the flags. Therefore a smaller D is disadvantageous to constant flapping of the flags. It seems that a separation distance that is approximately the flag total length (D between 0.7 and 0.8) is sufficient for the flapping leading flag to develop a fully fledged oscillating wake.

To find out how the range of transitional Reynolds number Re_t and the critical separation distance D_c may vary with the dimensionless bending modulus $\hat{K}_b$, several more sets of simulations were performed with the values of $\hat{K}_b$ decreased by ten times in one set of simulations and increased to $8.6 \times 10^{-3}, 4.7 \times 10^{-3}$ and 2.8×10^{-3} in other sets of simulations. The results are summarized in table 1. The first row lists the value of the dimensionless bending modulus, the second row lists the transitional Re range and the last row lists the interval where D_c is located. As we can see from

the table, the Re_t is not a linear function of $\hat{K}_b$. When $\hat{K}_b$ becomes ten times smaller, i.e. the flags are much more flexible, the Re transitional range becomes smaller accordingly (from 77–84 to 45–50). This may be explained by the fact that more flexible flags tend to flap more easily. The D_c is located in (0.9, 1.0). Note that the value of D_c is approximately the total length of the flag. When $\hat{K}_b$ becomes ten times lager, i.e. when the flags are much more stiff, the Re_t range is above 220. This remains true when $\hat{K}_b \geqslant 2.8 \times 10^{-3}$. The IB method we used for this work cannot solve the Navier – Stokes equations with a reasonable accuracy when Re is greater than a few hundreds, therefore we cannot find the Re transitional range and the corresponding value of D_c when $\hat{K}_b$ is sufficiently large, i.e. $\hat{K}_b \geqslant 2.8 \times 10^{-3}$. We did not try to find the Re_t and D_c for other smaller values of $\hat{K}_b$ because the computations are slow.

According to numerous simulations, it appears that for the self-sustained flapping to occur (for fixed $\hat{K}_b$), the Reynolds number has to be sufficiently large so that the inertial force dominates the viscous force. On the other hand, when Re is sufficiently small, the viscous force dominates and renders the flapping not sustainable. When the Re lies in a transitional range, presumably the inertial force and viscous force are of the same order; and it seems that the secondary effect of the separation distance D starts to dominate the flag dynamics. Therefore the flags can either flap constantly or be straight and static depending on D. Our simulations indicate that this is true for $\hat{K}_b$ in the range used in our work.

6. Summary and discussion

Previous laboratory measurements with tandem rigid bodies moving in a viscous fluid showed that it was more beneficial to follow than to lead in terms of the resistance the bodies encountered in the moving fluid. However, a very recent laboratory experiment with deformable bodies Ristroph & Zhang (2008) revealed just the opposite. Inspired by this experiment at high Re, we conduct a series of numerical computations on the drag of a pair of deformable flags placed in tandem in a flowing viscous incompressible fluid at moderate Re in the range of 40–220. Our simulations show that the drag relationship of the two flags depends on the Reynolds number. When Re is high enough, the two flags flap sustainedly, the drag of the leading flag is less than that of the following one (i.e. the inverted hydrodynamic drafting is observed); when Re is small enough, the flags maintain two stationary straight line segments, the drag of the following flag is less than the leading one (i.e. the hydrodynamic drafting is observed). These drag relationships hold for all the dimensionless parameters used in our work: separation distance $0 \leqslant D \leqslant 5.5$, Reynolds number $40 \leqslant Re \leqslant 220$, the flag bending rigidity $8.6 \times 10^{-5} \leqslant \hat{K}_b \leqslant 1.8 \times 10^{-3}$ and the flag mass $0.8 \leqslant \hat{M} \leqslant 1.0$. The transitional range of Re separating the differing drag relationships depends on the value of $\hat{K}_b$. For Re in the transitional range, either of the motion modes and drag relationships may occur depending on the separation distance D: if $D < D_c$, both flags are in the static straight line state and the downstream flag has less drag; if $D > D_c$, both flags are in the constant flapping state and the upstream flag has less drag. The critical separation distance D_c depends on $\hat{K}_b$. The ranges of Re_t and D_c are given for two specific values of $\hat{K}_b$.

One may argue that the inverted hydrodynamic drafting observed in the recent experiments Ristroph & Zhang (2008) and our simulations (the flapping case) is not surprising because the physical system in our problem is not the same as those in (Romberg *et al.* 1971; Zdravkovich 1977; Kyle 1979). On the surface of it, tandem flapping flags, tandem circular cylinders and queued race cars/bicyclists seem to be

different problems. However, all of these problems involve the complicated coupled interaction between the viscous fluid and the objects. This type of fluid-structure interaction is characterized by the interplay of fluid forces, body inertia and elasticity. The dynamics is controlled by the three dimensionless parameters: Re, $\hat{K}_b$ and $\hat{M}$. Therefore the differing phenomena may be explained by different values of these parameters. It seems that the inverted hydrodynamics drafting observed in the recent experiments and our simulations requires the immersed body be sufficiently flexible, i.e. $\hat{K}_b$ has to be small enough. When the body is sufficiently flexible, the shape of the body may be changed by the fluid forces. In the meantime, the changing shape may alter the fluid motion as well. Such interaction mediated by the change of body shapes may generate new phenomena different from the rigid case where the body shapes are fixed.

Our simulations indicate that the similar phenomenon discovered in the laboratory experiment at high Re ($\sim 10^4$) occurs as well at lower Re in the range of 50–220. In the meantime we also notice some differences in the results between Ristroph & Zhang (2008)'s and ours. First, the experimental values for $\hat{K}_b$ and $\hat{M}$ were 2.3×10^{-3} and 0.51, respectively. We find that flags with such values of $\hat{K}_b$ and $\hat{M}$ do not flap constantly for Re in 50–220: they always settle down to the static state. It is likely that this is because the Reynolds number is not high enough. Second, in the former work when Re was much higher the drag of each of the flags equalled approximately the drag of the single-flag case when D was greater than 5 (i.e. drag was approximately 1 when $D \geqslant 5$). In our case, however, while the drag of the trailing flag approximately equals 1, the drag of the leading flag is apparently greater than 1 when $D \geqslant 5$. Third, in our case the lower flag also experiences a drag reduction when $D = 0$ and 0.1. But in Ristroph and Zhang (2008)'s case, it did not happen. There could be two reasons behind these observed discrepancies. First, in the laboratory experiments the soap film was approximately 4.7 microns in thickness and the flag (rubber thread) was nearly 300 microns in diameter. So the actual physical problem in the experiments was a quasi-two-dimensional flow past a three-dimensional object. In contrast, in our simulations the flow is two-dimensional and the flags are one-dimensional flexible curves without volume which are totally immersed in the flow. Second, The Reynolds numbers in our simulations are approximately 200 times less than those in the experiments. Because of the high Re the flow in the laboratory experiments was probably turbulent. In our simulations the Reynolds numbers are significantly lower. The velocity field from our simulations at $Re = 220$ does not show any fluctuations in space and time (the plots of $\mathbf{u}(x, y, t)$ are not highly oscillatory in x, y and t). This seems to suggest that the flows in our simulations are laminar. Therefore it seems unlikely that the critical Re_t found in our work would correspond to a transition from laminar to turbulent when Re is increased from 40 to 220. Note that our numerical method for the Navier–Stokes equations is independent of the nature of the flow as long as the Re is roughly less than a couple of hundred. The uncertain nature of the flow does not affect the accuracy of our numerical results.

The drag of the flag may be roughly classified into two categories: form drag and skin-friction drag (here the induced drag is treated as part of the form drag). The friction drag is defined as the y component of the total force due to the tangential stress exerted by the fluid on the flag. It is caused by the fluid viscosity. The form drag is defined as the y component of the resultant pressure difference on the leading and trailing edges of the flag (in flapping case). It strongly depends on the shape of the flag. Presumably the form drag dominates the total drag if the Reynolds number is large enough and the skin-friction drag dominates the total drag if the Reynolds

number is small enough. The ratio of the form drag over the skin-friction drag signifies the relative importance of the two types of drag. While in the non-flapping case the flags are nearly stationary and the shape drag is not thought to be important, it seems that both the shape and friction drag are important in the flapping case. It would be interesting to compute separately the two types of drag for the flapping case. However, we did not obtain such a decomposition sufficiently accurately. Interested readers may refer to a very recent publication by Williams, Fauci & Gaver (2009) for how this may be done.

We may speculate that when the separation distance D is sufficiently large the interaction between the two flags would become so weak that the drag of each flag would equal to 1. When Re is very high, the critical D is approximately 5 Ristroph & Zhang (2008). It appears that the critical value of D depends on Re and is larger at lower Re. Because of limitations in the size of the computational domain (increase of the size has to be accompanied by the increase of grid points), we are not able to identify such values for D at lower Reynolds numbers.

Our work has focused on the interaction and the resultant drag relationship of two tandem flags separated by a distance solely in the longitudinal direction (y direction). Presumably a finite lateral separation distance may change the interaction between the flags and alter the drag relationship. It would be an interesting piece of future work to investigate the interaction and drag relationship of two flags separated in both longitudinal and lateral directions.

There are three important dimensionless parameters in our problem: the Reynolds number Re, the flag bending modulus $\hat{K}_b$ and the flag mass density $\hat{M}$. (In all of our simulations the flag stretching/compression coefficient $\hat{K}_s$ and the Froude number Fr are kept fixed. The $\hat{K}_s$ is chosen such that the flags are almost inextensible. It is assumed that the influence of $\hat{K}_s$ and Fr are not important.) Presumably, the drag relationship would depend on these dimensionless parameters. The results of our work are based on the simulations with these parameters in certain ranges: Re in 40–220, $\hat{K}_b$ in 8.6×10^{-4}–1.8×10^{-3}, $\hat{M}$ in 0.8–1.0. Because of these three controlling dimensionless parameters, the seemingly simple two-flag-fluid system is in fact quite complicated in nature. There may exist other transitions corresponding to the critical values of other parameters such as $\hat{K}_b$. To obtain a comprehensive understanding of this system, we need a complete picture of the transitions associated with each critical value of these dimensionless parameters. It would be interesting to explore the whole three-dimensional parameter space (Re, $\hat{K}_b$, $\hat{M}$) for an exhaustive parametric study. However, this is out of question at the time being because the computations are pretty slow. Even a less ambitious task – a parametric study on the two-dimensional (Re, $\hat{K}_b$) half-plane ($Re \leqslant 220$) may well take more than one year to accomplish given the fastest computers at our dispose. We have to postpone this piece of work to the future.

The author thanks Jun Zhang for helpful discussion on the laboratory experiment and findings, and thanks the three unknown referees whose comments and suggestions have made the paper better. The author thanks the USA National Science Foundation for the support under the research Grant DMS-0713718.

REFERENCES

Alben, S., Shelley, M. & Zhang, J. 2002 Drag reduction through self-similar bending of a flexible body. *Nature* **420**, 479–481.

Argentina, M. & Mahadevan, L. 2005 Fluid-flow induced flutter of a flag. *PNAS* **102**, 1829.

Atzberger, P. J., Kramer, P. R. & Peskin, C. S. 2006 A stochastic immersed boundary method for biological fluid dynamics at microscopic length scale. *J. Comput. Phys.* **224** (2), 1255–1292.

Bell, J. B., Colella, P. & Glaz, H. M. 1989 A second order projection method for the incompressible Navier–Stokes equations. *J. Comput. Phys.* **85**, 257.

Bell, J. B., Colella, P. & Howell, L. H. 1991 An efficient second-order projection method for viscous incompressible flow. In *Proceedings of the Tenth AIAA Computational Fluid Dynamics Conference*, Honolulu, June 24–26 (USA).

Bill, R. G. & Herrnkind, W. F. 1973 Drag reduction by formation movement in spiny lobsters. *Science* **193**, 1146–1148.

Borazjani, I., Ge, L. & Sotiropoulos, F. 2008 Curvilinear immersed boundary method for simulating fluid structure interaction with complex three-dimensional rigid bodies. *J. Comput. Phys.* **227** (16), 7587–7620.

Botella, O. 1997 On the solution of the Navier–Stokes equations using Chebyshev projection schemes with third-order accuracy in time. *Comput. Fluids* **26**, 107.

Brown, D. L., Cortez, R. & Minion, M. L. 2001 Accurate projection methods for the incompressible Navier–Stokes equations. *J. Comput. Phys.* **168** (2), 464.

Chorin, A. J. 1968 Numerical solution of the Navier–Stokes equations. *Math. Comput.* **22**, 745.

Chorin, A. J. 1969 On the convergence of discrete approximations to the Navier–Stokes equations. *Math. Comput.* **23**, 341.

Connell, B. S. H. & Yue, D. K. P. 2007 Flapping dynamics of a flag in a uniform stream. *J. Fluid Mech.* **581**, 33–67.

Cottet, G. H. & Maitre, E. 2004 A level set formulation of immersed boundary methods for fluid-structure interaction problems. *C. R. Acad. Sci. Paris, Ser.* I **338**, 581–586.

Cottet, G. H. & Maitre, E. 2006 A level set method for fluid-structure interactions with immersed interfaces. *Math. Models Methods Applied Sci.* **16**, 415–438.

Donea, J. Giuliani, S. & Halleux, J. P. 1982 An arbitrary Lagrangian–Eulerian finite element method for transient dynamic fluid structure interactions. *Comput. Methods Appl. Mech. Engng* **33**, 689.

Dong, G.-J. & Lu, X.-Y. 2007 Characteristics of flow over travelling wavy foils in a side-by-side arrangement. *Phys. Fluids* **19**, 057107.

Farnell, D. J. J., David, T. & Barton, D. C. 2004 Coupled states of flapping flags *J. Fluids Struct.* **19**, 29–36.

Fauci, L. J. 1990 Interaction of oscillating filaments: a computational study. *J. Comput. Phys.* **86**, 294–313.

Fauci, L. J. & Fogelson, A. L. 1993 Truncated Newton methods and the modelling of complex elastic structures. *Commun. Pure Appl. Math.* **46**, 787.

Fauci, L. & Peskin, C. S. 1988 A computational model of aquatic animal locomotion. *J. Comput. Phys.* **77**, 85–108.

Fedkiw, R. P. 2002 Coupling an Eulerian fluid calculation to a Lagrangian solid calculation with the ghost fluid method. *J. Comput. Phys.* **175** (1), 200–224.

Fedkiw, R. P., Aslam, T., Merriman, B. & Osher, S. 1999 A non-oscillatory Eulerian approach to interfaces in multimaterial flows (the ghost fluid method). *J. Comput. Phys.* **152** (2), 457–492.

Fogelson, A. L. & Peskin, C. S. 1988 A fast numerical method for solving the three-dimensional Stokes' equations in the presence of suspended particles. *J. Comput. Phys.* **79**, 50–69.

Glowinski, R., Pan, T., Hesla, T., Joseph, D. & Periaux, J. 2001 A fictitious domain approach to the direct numerical simulation of incompressible viscous flow past moving rigid bodies: application to particulate flow. *J. Comput. Phys.* **169**, 363.

Glowinski, R., Pan, T. & Periaux, J. 1994*a* A fictitious domain method for Dirichlet problem and applications. *Comput. Methods Appl. Mech. Engng* **111**.

Glowinski, R., Pan, T. & Periaux, J. 1994*b* A fictitious domain method for external incompressible viscous flow modelled by Navier–Stokes equations. *Comput. Methods Appl. Mech. Engng* **112**.

Griffith, B. E. & Peskin, C. S. 2005 On the order of accuracy of the immersed boundary method: higher order convergence rates for sufficient smooth problems. *J. Comput. Phys.* **208** (1), 75–105.

Hou, T. Y., Li, Z. L., Osher, S. & Zhao, H. K. 1997 A hybrid method for moving interface problems with application to the Hele–Shaw flow. *J. Comput. Phys.* **134**, 236–252.

Hughes, T. J. R., Liu, W. & Zimmerman, T. K. 1981 Lagrangian–Eulerian finite element formulation for incompressible viscous flows. *Comput. Methods Appl. Mech. Engng* **29**.

Jia, L. B., Li, F., Yin, X. Z. & Yin, 2007 Coupling modes between two flapping filaments. *J. Fluid Mech.* **581**, 199–220.

Kim, Y. & Peskin, C. S. 2007 Penalty immersed boundary method for an elastic boundary with mass. *Phys. Fluids* **19** (5), 053103.

Kyle, C. R. 1979 Reduction of wind resistance and power output of racing cyclists and runners travelling in groups. *Ergonomics* **22**, 387–397.

Lai, M. C. & Peskin, C. S. 2000 An immersed boundary method with formal second order accuracy and reduced numerical viscosity. *J. Comput. Phys.* **160**, 705.

LeVeque, R. J. & Li, Z. L. 1994 The immersed interface method for elliptic equations with discontinuous coefficients and singular sources. *SIAM J. Numer. Anal.* **31**, 1019–1044.

LeVeque, R. J. & Li, Z. L. 1997 Immersed interface methods for Stokes flows with elastic boundaries or surface tension. *SIAM J. Sci. Comput.* **18**, 709–735.

Li, Z. L. 2006 *The Immersed Interface Method – Numerical Solutions of PDEs Involving Interfaces and Irregular Domains*. SIAM.

Li, Z. L. & Lai, M. C. 2001 Immersed interface methods for Navier–Stokes equations with singular forces. *J. Comput. Phys.* **171**, 822–842.

Liao, J. C., Beal, D. N., Lauder, G. V. & Triantafyllou, M. S. 2003 The Kármán gait: novel body kinematics of rainbow trout swimming in a vortex street. *J. Exp. Biol.* **206**, 1059.

Liu, W. K., Kim, D. K. & Tang, S. 2006 Mathematical foundations of the immersed finite element method. *Comput. Mech.*, **39** (3), 211–222.

Lopez, J. M., Marques, F. & Shen, J. 2002 An efficient spectral-projection method for the Navier–Stokes equations in cylindrical geometries II. Three-dimensional cases. *J. Comput. Phys.* **176** (2), 384–401.

Lopez, J. M. & Shen, J. 1998 An efficient spectral-projection method for the Navier–Stokes equations in cylindrical geometries I. Axisymmetric cases. *J. Comput. Phys.* **139** (2), 308–326.

Mittal, R. & Iaccarino, G. 2005 Immersed boundary methods. *Annu. Rev. Fluid Mech.* **37**, 239–261.

Mori, Y. & Peskin, C. S. 2008 Implicit second-order immersed boundary method with boundary mass. *Comput. Methods Appl. Mech. Eng.* **197**, 1213–1263.

Perot, J. B. 1993 An analysis of the fractional step method. *J. Comput. Phys.* **108**, 51.

Peskin, C. S. 1977 Flow patterns around heart valves: a numerical method. *J. Comput. Phys.* **25**, 220.

Peskin, C. S. 2002 The immersed boundary method. *Acta Numerica* **11**, 479.

Peskin, C. S. & McQueen, D. M. 1993 Computational biofluid dynamics. *Contemp. Math.* **141**, 161.

Qi, D. & Shyy, W. Submitted Simulations of dynamics of free falling of flexible fibres in moderate Reynolds number flows. *J. Fluid Mech.*

Ristroph, L. & Zhang, J. 2008 Anomalous hydrodynamic drafting of interacting flapping flags. *Phys. Rev. Lett.* **101**, 194502.

Roma, A. M., Peskin, C. S. & Berger, M. J. 1999 An adaptive version of the immersed boundary method. *J. Comput. Phys.* **153**, 509–534.

Romberg, C. F., Chianese, Jr., F. & Lajoie, R. G. 1971 Aerodynamics of race cars in drafting and passing situations. *Soc. Auto. Engng* 710213.

Sheldon Wang, X. 2007 An iterative matrix-free method in implicit immersed boundary/continuum methods. *Comput. Struct.* **85**, 739–748.

Shelley, M., Vandenberghe, N. & Zhang, J. 2005 Heavy flags undergo spontaneous oscillations in flowing water. *Phys. Rev. Lett.* **94** (9), 094302.

Sulsky, D., Chen, Z. & Schreyer, H. L. 1994*a* A particle method for history-dependent materials. *Comput. Mech. Appl. Mech. Engng* **118**, 179–197.

Sulsky, D., Zhou, S. J. & Schreyer, H. L. 1994*b* Application of a particle-in-cell method to solid mechanics. *Comput. Phys. Commun.* **87**, 136–152.

Wang, X. 2006 From immersed boundary method to immersed continuum method. *Intl J. Multiscale Comput. Engng* **4** (1), 127–145.

Wang, X. & Liu, W. K. 2004 Extended immersed boundary method using FEM and RKPM. *Comput. Methods Appl. Mech. Engng*, **193** (12-14), 1305.

Weinan, E. & Liu, J.-G. 1995 Projection method I: convergence and numerical boundary layers. *SIAM J. Numer. Anal.* **32**, 1017.

Weinan, E. & Liu, J.-G. 1996 Projection method II: Godunov–Ryabenki analysis. *SIAM J. Numer. Anal.* **33**, 1597.

Williams, H. A. R., Fauci, L. J. & Gaver, D. P. 2009 Evaluation of interfacial fluid dynamical stresses using the immersed boundary method. *Discrete Continuous Dyn. Syst., Ser.* B **11** (2), 519–540.

Xu, J., Li, Z., Lowengrub, J. & Zhao, H. 2006 A level set method for interfacial flows with surfactant. *J. Comput. Phys.* **212** (2), 590–616.

Zdravkovich, M. M. 1977 Review of flow interference between two circular cylinders in various arrangement. *J. Fluids Engng* **99**, 618–633.

Zhang, J., Childress, S. Libchaber, A. & Shelley, M. 2000 Flexible filaments in a flowing soap film as a model for one-dimensional flags in a two-dimensional wind. *Nature* **408**, 835.

Zhang, L., Gersternberger, A., Wang, X. & Liu, W. K. 2004 Immersed finite element method. *Comput. Methods Appl. Mech. Engng* **193**, 2051.

Zhu, L. 2008 Scaling law for drag of a flexible object moving in an incompressible viscous fluid. *J. Fluid Mech.* **607**, 387–400.

Zhu, L. & Chin, R. 2008 Simulation of elastic filaments interacting with a viscous pulsatile flow. *Comput. Method Appl. Mech. Engng* **197**, 2265–2274.

Zhu, L. & Peskin, C. S. 2002 Simulation of a flexible flapping filament in a flowing soap film by the immersed boundary method. *J. Comput. Phys.* **179** (2), 452–468.

Zhu, L. & Peskin, C. S. 2003 Interaction of two flexible filaments in a flowing soap film. *Phys. Fluids* **15** (7), 1954–1960.